



Department of Physics,
University College Cork,
Ireland
PY4115 - Major Research Project
Final report

Photon emission processes from site-controlled quantum dots.

Eoin Murray

110367833

Supervisor: Dr. Emanuele Pelucchi

April 4, 2014.

Abstract

Research on the practical realisation of quantum computing and quantum information science is proceeding expeditiously. Presented in this work is an approach using quantum dots (QDs) as a photonic qubit source. Quantum dots are commonly referred to as “artificial atoms” due to their discrete energy levels and few carrier confinement. They allow on demand qubits and compatible with semiconductor foundry technologies. An inexpensive solid state device capable of generating single and entangled qubits on demand would be a great asset in exploring practical quantum technologies.

In practice the barrier to perfect entangled photon emission is the fine structure splitting (FSS) and decoherence. In this report it is verified that all photon pairs emitted from the biexciton cascade are entangled. However a time dependent phase when the FSS is non-zero causes the measured ensemble to be made of non-identical pairs, and thus the results can look non-entangled.

In this report is a detailed study on a charged biexciton species observed in the entangled photon emitting QDs is also presented. This specific species is a good indicator that the QD is an entangled photon emitter. A theoretical fine structure is presented supported by correlation measurements and a rate equation model.

Acknowledgements

Many thanks to Dr. Emanuele Pelucchi for hosting me in his group over the course of this project. I have learned a great deal during my time with his group. Thanks also to all the group members who grew the samples. Special thanks to Dr. Gediminas Juska, with whom this work was done.

Contents

1	Introduction	9
1.1	Quantum dot electronic structure.	9
1.2	Exciton fine-structure and entanglement.	10
1.3	Fine structure splitting.	13
2	Methods	16
2.1	Sample preparation.	16
2.2	Spectroscopy.	19
2.3	Photon correlation measurements.	20
2.4	Modelling the experiment.	22
3	Time resolved entanglement	27
3.1	Theory of time gating.	27
3.2	Experimental data.	29
3.2.1	Fidelity versus gate start time.	30
3.2.2	Fidelity versus gate width.	31
3.3	Simulation results.	32
4	Charged biexciton states	35

4.1	Theory	35
4.2	Experimental and modelling	37
5	Conclusions and further work	42
6	Appendix 1	43
	References	48

1 Introduction

Quantum dots are semiconductor islands capable of zero-dimensionally confining electronic charge carriers. This confinement gives rise to discrete energy levels in the dot. Due to their discrete energy levels, quantum dots are commonly known as “artificial atoms”. Quantum dots are good candidates as the active qubit source in many potential quantum information solid state technologies [4]. Current quantum dot manufacturing technology has the potential to be applied on an industrial scale, however more research needs to be done to refine the quantum dot properties. Control of quantum dot behaviour and higher uniformity and symmetry need to be achieved before they can be adopted for wide spread use.

1.1 Quantum dot electronic structure.

Quantum dots (QDs) are three dimensional semiconductor regions contained within semiconductor of a higher bandgap. The QDs confine the electronic carriers in three dimensions, this confinement give rise to discrete energy levels in the dot. The energetic separation between the levels and the amount of carriers that can be confined depend on the shape and size of the QD.

Typically one or two electron levels and one or two hole levels exist in the dot. Larger QDs may accommodate more carriers. Due to the Pauli exclusion principle each energy level can accommodate only two carriers, of opposite spins, as shown in Figure 1. The coulomb repulsion and attraction also have a major role in determining the exact energy levels in the dot.

Electrons and holes are created in or near the dot by electro- or photo-excitation. Electrons are excited into the conduction band and holes are left in the valence band. An e-h pair is referred to as an exciton. Typically, mobile carriers are created in the bulk material by above band excitation and they relax into different confinement

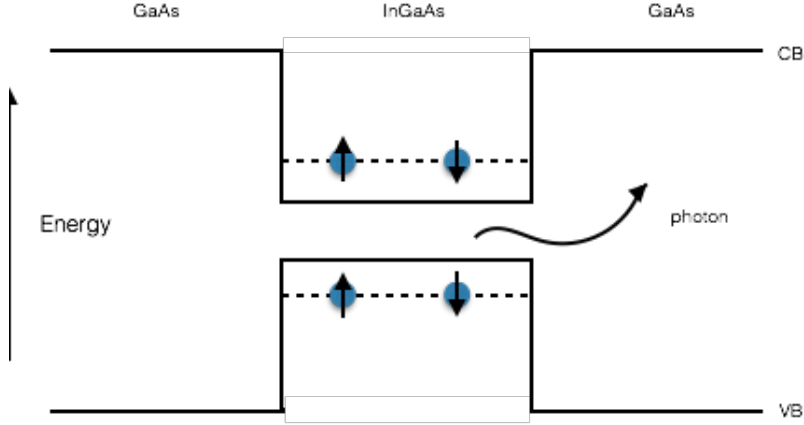


Figure 1: Energetic structure of the biexciton

potentials in the heterostructure. The QD will normally be the lowest energy confinement. This scheme is useful because it allows the dot to be populated by lasers at a lower wavelength than the dot emission wavelength. Thus the exciting laser and dot are spectrally separated and can be identified experimentally.

Several excitonic complexes can form inside the QD. A single e-h pair is an exciton, a double e-h pair is a biexciton. An unbalance in the number of electrons and holes can cause charge excitonic complexes. For example a single electron and two holes creates an exciton with an extra hole in the dot, this is referred to as a positively charged exciton, or positive trion. The photoluminescence spectrum of each complex is different due to the Coulomb interaction between the carriers. The spectrum of the entire QD can be made up of many peaks and identifying each peak can be done by power dependence measurements and/or photon correlation measurements.

1.2 Exciton fine-structure and entanglement.

An electron has spin $\pm 1/2$ and a heavy hole has spin $\pm 3/2$ (light holes occupy higher energy levels and are ignored in the scope of this work). Thus an e-h pair, an exciton, confined in the dot has total angular momentum projected along the \hat{z} -axis M_z of ± 1 or ± 2 .

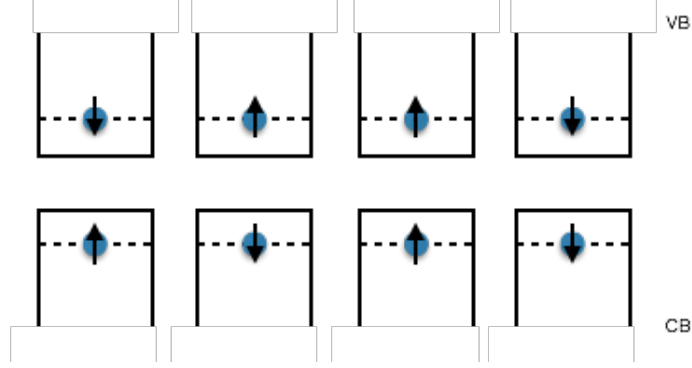


Figure 2: Energetic structure of the exciton, showing the four different spin configurations.

Excitons with $M_z = \pm 1$ can optically recombine and are referred to as bright states. For excitons with $M_z = \pm 2$ optical recombination is forbidden and are called dark states. Dark states only emit a photon if a spin flip occurs.

Due to the exchange interaction between the electron and hole, the fourfold degenerate exciton state, turns into a pair of twofold degenerate states. One with $M_z = \pm 1$ and one with $M_z = \pm 2$. The $M_z = \pm 2$ case is energetically lower, due to the aligned spins of the electron and hole.

The biexciton consists of a pair of anti-aligned electrons and holes, it thus has no total angular momentum. It is a single degenerate state because there is no exchange interaction.

Since the total angular momentum of the biexciton is zero, it cannot recombine directly to the ground state, it can only relax to the ground state through an intermediary state by changing the angular momentum by ± 1 . As the biexciton decays to the exciton an angular momentum change of $+1$ (-1) occurs, emitting a right (left) hand circularly polarised photon. As the exciton then decays to the ground state the opposite angular momentum change must occur so the change is $-1(+1)$, emitting a left (right) hand circularly polarised photon. This transition is shown schematically in Fig 3.

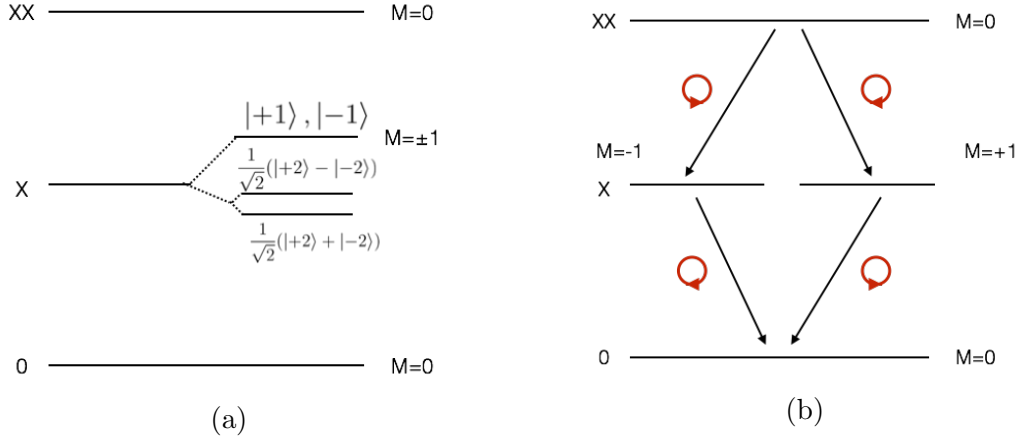


Figure 3: (a) The fine structure of the exciton and (b) the recombination cascade of the biexciton. The biexciton is a singlet state with no angular momentum $M = 0$, the exciton has angular momentum $M = \pm 1$ and the empty dot has $M = 0$.

No path is preferential and no which path information can be determined until a measurement of the emitted photons. The initial electronic state of the biexciton is that of a singlet state, it is in the superposition of indistinguishable opposing spin excitons. This entanglement between the exciton and biexciton should be retained in the emitted photons. This singlet state can be represented by:

$$|\psi\rangle = \frac{1}{\sqrt{2}} (|\uparrow\downarrow\rangle + |\downarrow\uparrow\rangle). \quad (1.1)$$

After emission the state is in the superposition of the left and right circularly polarised photons, giving rise to photon polarization entanglement:

$$|\psi\rangle = \frac{1}{\sqrt{2}} (|L_{XX}R_X\rangle + |R_{XX}L_X\rangle). \quad (1.2)$$

Which is equivalent to

$$|\psi\rangle = \frac{1}{\sqrt{2}} (|H_{XX}H_X\rangle + |V_{XX}V_X\rangle). \quad (1.3)$$

In the rectilinear basis (H (V) - horizontal (vertical) polarised photon). This recombination cascade is presented schematically in Figure 3. This state is one of the maximally entangled Bell states $|\Psi^+\rangle$.

1.3 Fine structure splitting.

In real QD systems however, the degeneracy of the bright exciton state is lifted due to a multitude of effects. If the confinement potential symmetry is low then e-h exchange interaction causes the exciton level to split.

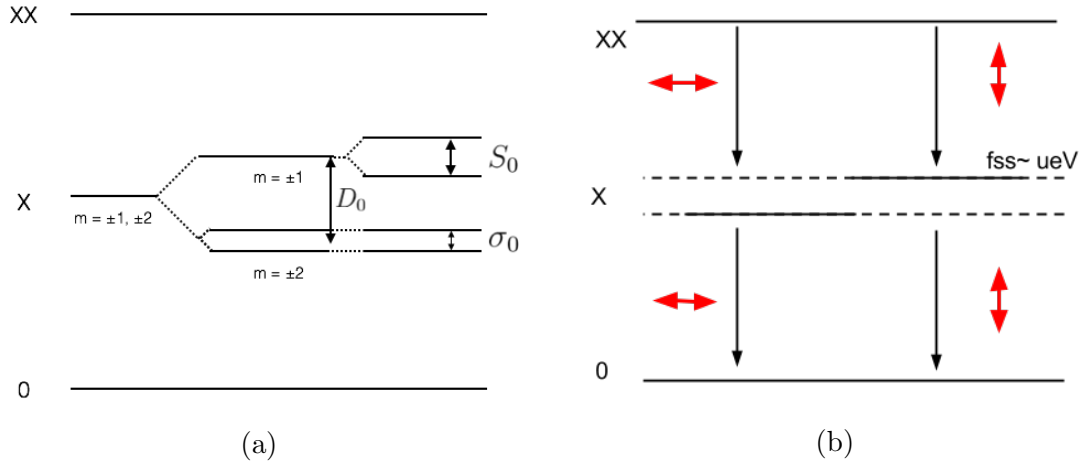


Figure 4: (a) The fine structure of the exciton with lifted degeneracy and (b) the two optical decay paths when the dot exhibits fine structure splitting.

This loss of symmetry can be caused by elongation of the QD, strain, random alloy segregation or piezoelectric fields in the vicinity of the dot. When this degeneracy lifting occurs the non-degenerate exciton levels are split by an energy amount called the fine-structure splitting (FSS). For the biexciton state e-h exchange interaction does not occur and it remains a single state. Since the biexciton cascade must propagate through the exciton state, and there is time evolving mixing of the exciton non-degenerate levels. This new cascade is shown in Figure 4. With respect to the emitted photons, the FSS modifies the entanglement [14]. The biexciton cascade proceeds as follows. The dot is first populated with a biexciton:

$$|\psi\rangle = \frac{1}{\sqrt{2}} (|XX_HX_H\rangle + |XX_VX_V\rangle). \quad (1.4)$$

When the biexciton decays to the exciton state, a photon is emitted of horizontal (H) or vertical (V) polarisation. The QD state becomes a superposition of the emitted biexciton photon and the exciton remaining in the dot. The non-degenerate exciton states evolve at different rates, the difference being proportional to the size of the FSS. The state is then:

$$|\psi\rangle = \frac{1}{\sqrt{2}} \left(|H_{XX}X_H\rangle + e^{\frac{iFSS}{\hbar}t} |V_{XX}X_V\rangle \right). \quad (1.5)$$

The phase rotates the state until the exciton is emitted after time τ_Δ . The final emitted photonic state is then:

$$|\psi\rangle = \frac{1}{\sqrt{2}} \left(|H_{XX}H_X\rangle + e^{\frac{iFSS}{\hbar}\tau_\Delta} |V_{XX}V_X\rangle \right). \quad (1.6)$$

The biexciton and exciton emission lifetimes vary according to decaying exponential distributions and as such so will τ_Δ . When the FSS of the QD is non-zero this varying term τ_Δ can cause the phase of the state to average out to zero, and thus measurements of the state will look non-entangled.

Entanglement measurements are evaluated on an ensemble of identical states. In the regime of non-zero FSS however, the state is still entangled, the states are not identical, and the phase term changes in each occurrence of emitted pairs. In measurements the overall state looks mixed with the entanglement degraded. Good entanglement detection therefore depends on the parameter $e^{\frac{iFSS\tau_\Delta}{\hbar}}$. If we can make the FSS to be zero or almost zero therefore we can approach the regime of ideal entanglement. Much research has gone into quantum dot systems that control or minimise the FSS [12, 13]. However creating QDs with perfect zero FSS is difficult.

Another approach would be to select only the emitted photons where τ_{Δ} is at a pre-determined value [14]. In this case we can select pairs with a certain phase. This method is called time-tagging. In theory we can time-tag to prefer multiple maximally entangled states, for example $\frac{1}{\sqrt{2}}(|HH\rangle \pm |VV\rangle)$, or $\frac{1}{\sqrt{2}}(|HH\rangle \pm i|VV\rangle)$. Selecting different states however is done at the cost of lower intensity due to the exciton lifetime decaying with exponentially decaying intensity.

2 Methods

In this chapter the manufacturing and experimental methods used to create and categorise the QD's are documented. It should be noted that the author of this report focused exclusively on the experimental and theoretical work, and did not manufacture any of the samples. The manufacturing is described for understanding and also to present the advantages of the site controlled system.

2.1 Sample preparation.

In this section the manufacturing methods for the site controlled system will be documented. The advantage of this system is precise control of parameters of the grown QD's. The manufacturing steps are also compatible with existing semiconductor foundry techniques.

Prepatterning. The GaAs (111)B substrates are prepatterned with inverted pyramids by typical UV lithography and wet chemical etching procedures. A thin layer of SiO₂ and photoresist are layered on the top of the substrate. The triangular pattern is then transferred from a chrome mask to the photoresist by exposure to a UV lamp and development in a MF-319 solution. This pattern is transferred to the SiO₂ using hydrofluoric acid. A Br:Methanol solution is used to etch into the GaAs, where the anisotropy of the etch between the (111)A and (111)B surfaces results in the inverted pyramid being inserted into the substrate. The profile of the substrate is now of a periodic array of inverted pyramids. Peak to peak distance between pyramids is 7.5 μ m.

MOVPE Growth. The semiconductor layers were grown on the patterned substrate by Metalorganic vapour phase epitaxy (MOVPE). MOVPE growth is complex

and will not be described in detail here. The epitaxial layers grown is as follows:

1. A thin GaAs buffer layer.
2. A protective $\text{Al}_{0.75}\text{Ga}_{0.25}\text{As}/\text{GaAs}$ layer.
3. Double barrier structures of $\text{Al}_{0.55}\text{Ga}_{0.45}\text{As}/\text{GaAs}$.
4. GaAs.
5. Active $\text{In}_x\text{Ga}_{1-x}\text{As}/\text{GaAs}$ layer.

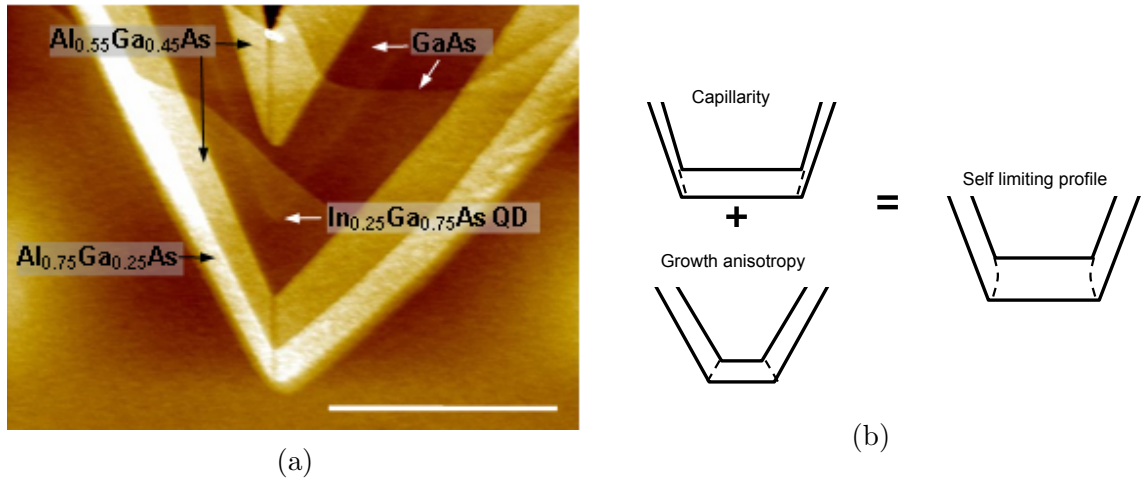


Figure 5: (a) AFM image¹ of a cleaved pyramid showing the epitaxially grown semiconductor layers. (b) Self limiting profile formation that gives rise to the QD shape at the tip of the pyramid caused by the capillarity and growth anisotropy effects described in the text.

An AFM image of these layers is shown in Figure 5 (a). QDs are self-formed at the central axis of the $\text{In}_x\text{Ga}_{1-x}\text{As}/\text{GaAs}$ layer. The properties of the QD growth depend on the equilibrium of the growth anisotropy and capillarity effects. Growth anisotropy is due to the differing growth rates on the (111)A surface on the faces of the pyramids and the (111)B surface at the bottom, it increases the growth rate on the pyramid faces. The capillarity effect is due to adatoms diffusing to reduce surface energy by increasing planarity, thus they tend to diffuse to the bottom of the pyramid, it increases the growth rate at the bottom (the tip in the apex down geometry) of

¹Courtesy of the EPN group.

the pyramid. The equilibrium of these process gives rise to the self limiting profile of the QD layer. This is shown schematically in Figure 5 (b).

The advantage of the MOVPE growth is that the self limiting profile that dictates the QD shape and size, which in turn change the emission wavelength and exciton-biexciton binding energy etc., can be altered by changing growth temperature and alloy composition.

Surface etching. The pyramids are still in the apex down geometry. The surface etching is primarily to increase the quality of the emission spectrum, some irregularities that form at the top of the sample can be confusing in the optical spectrum. The sample is layered with photoresist, then oxygen plasma partially etches away the photoresist until the irregularities are uncovered but photoresist remains in the pyramid. The irregularities are then etched away with sulfuric acid and peroxide.

Back etching. This procedure ‘flips’ the pyramids into a free standing apex up geometry. The pyramid acts as a lens that decreases internal reflections and the and enhances the emission collection by up to three orders of magnitude. The lens gives the emitted photons a preferential ‘up’ direction towards the collection aperture. Another support substrate is prepared with strips of titanium and gold on the surface. A titanium and gold layer is evaporated onto the original sample.

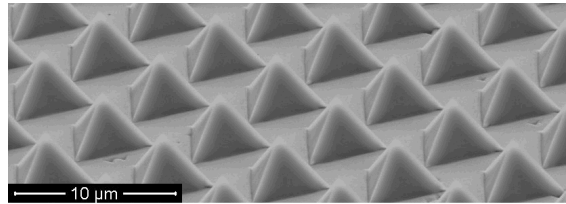


Figure 6: SEM image² of the free standing pyramids after back etching.

The two substrates are attached thermo-compression gold bonding. The strips allow air to escape when the sample is cooled to $\sim 8\text{K}$. The original substrate is etched

²Courtesy of the EPN group.

away by different chemical solutions. The etching rate of the $\text{Al}_{0.75}\text{Ga}_{0.25}\text{As}/\text{GaAs}$ layer on the pyramid is much slower than that of GaAs, so that the QD layers are protected. An scanning electron microscopy image of these free standing pyramids is shown in Figure 6.

2.2 Spectroscopy.

Optical characterisation of single pyramids is done with a standard micro photoluminescence setup (see Figure 7). A continuous wave (cw) laser diode ($\lambda=658\text{nm}$) or pulsed laser diode ($\lambda=650\text{nm}$) can be used to excite the QD. The cw laser allows higher emission intensity because the QD is immediately repopulated after relaxation. The pulsed laser is used for time-resolved measurements. High magnification (100x) of the sample surface is achieved using a small working distance of the objective. The laser beam is focused to a point on the sample smaller than the area of a single pyramid. Before the QD emission is sent to the spectrometer the laser light is filtered by a long-pass filter. The filtered emission is then sent to the spectrometer equipped with a charge-coupled device (CCD) or InGaAs detector array.

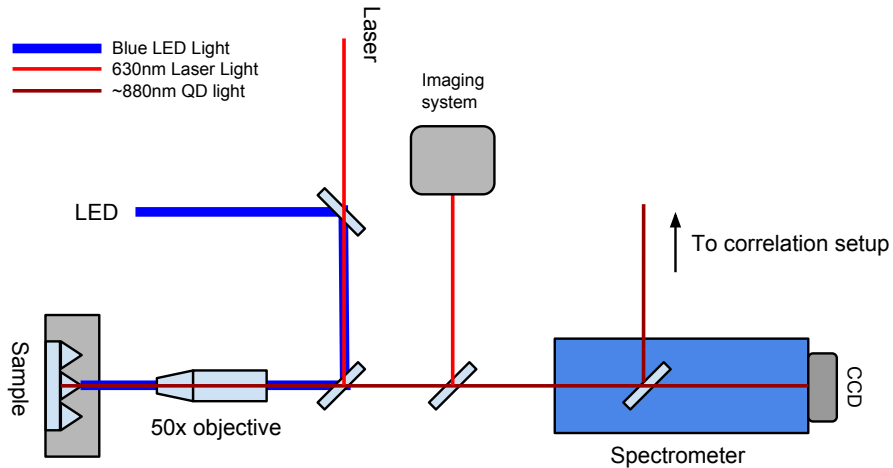


Figure 7: Schematic of the micro photoluminescence setup.

The sample is mounted in a closed-cycle helium cryostat and the temperature used for measurement is typically 8K. A blue LED can be used to illuminate the sample.

By placing a beamsplitter in the optical axis the image of the sample surface is sent to the CCD. This allows simultaneous imaging of the sample surface and measurement of the photoluminescent spectrum. This is typically used to find a candidate QD for further measurements. The beamsplitter is removed during measurements to increase collection efficiency.

Measurements of the FSS were carried out by placing a half-wave plate and a linear polarizer in-line with the emission axis, between the QD source and spectrometer. The FSS causes the energetic/spectral positions of the exciton and biexciton transitions follow counter phase sinusoids while changing polarization angle. The sinusoidal curve is obtained by subtracting the biexcitons energy from the excitons. The amplitude of the sinusoid has the value of FSS.

For time-resolved measurements such as measuring the lifetimes and correlations avalanche photo diodes (APDs) and photon counting modules (PCMs) are used. The spectrometer can work as a monochromator and an internal lateral mirror sends the selected wavelength through an exit slit towards the APDs. APDs can detect single photons and are synced with the PCM to give the arrival time of the photons in the lifetime measurements. The histogram of such arrival times gives the photoluminescent decay curves from which the state lifetime can be determined.

2.3 Photon correlation measurements.

Polarisation resolved correlation measurements are carried out in a Hanbury Brown and Twiss (HBT) setup. The experiment schematic is presented in Figure 8. The QD emission stream is sent towards a non-polarising 50:50 beam splitter. A polarisation projection is chosen using a combination of half and quarter waveplates. The exciton and biexciton photons are energetically different and they discriminated using monochromators. Each filtered photon was selected by a polarizing beamsplitter and sent to avalanche photodiodes detectors (APDs). Two APDs are used in each chan-

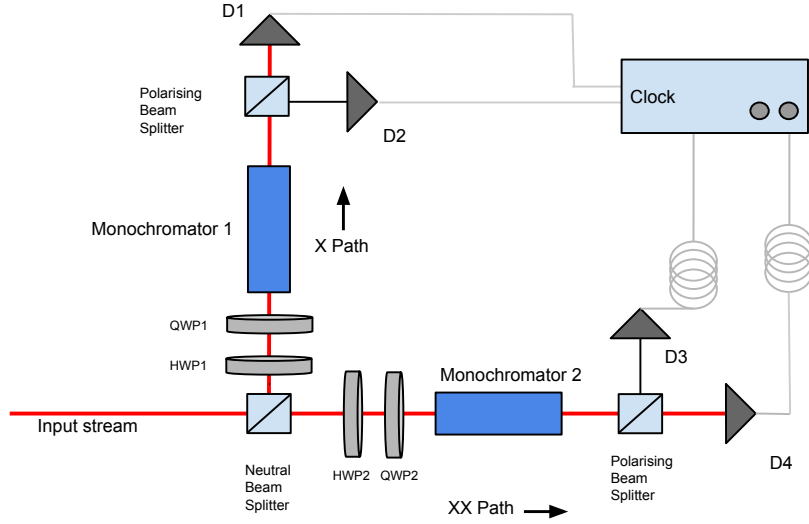


Figure 8: Schematic of the Hanbury Brown Twiss correlator.

nel, one starts a counting module, the other stops it. The stop event is electrically delayed in order to obtain negative correlation values. The obtained curves represent the second order correlation function $g^{(2)}(\tau)$ (see Ref. [7] for a good introduction).

$$g_{ij}^{(2)}(\tau) = \frac{\langle I_i(t) I_j(t + \tau) \rangle}{\langle I_i(t) \rangle \langle I_j(t + \tau) \rangle} \quad (2.1)$$

Where $I_n(t)$ is the intensity of state n at time t . $g^{(2)}(\tau)$ represents the conditional probability of a j -th excitonic transition photon to be measured at the time τ after the i -th excitonic transition photon is measured. Four synchronized sequences of detector signals were used to build four correlation curves. By choosing different polarisation bases (Typically rectilinear, diagonal and circular) and measuring $g^{(2)}(\tau)$, the biexciton-exciton photon entanglement can be categorised. The degree of correlation in each basis can be calculated by $C = \frac{g_{\parallel}^{(2)}(0) - g_{\perp}^{(2)}(0)}{g_{\parallel}^{(2)}(0) + g_{\perp}^{(2)}(0)}$. Where $g_{\parallel}^{(2)}(\tau)$ is the $g^{(2)}$ value for co-polarised pairs and $g_{\perp}^{(2)}(\tau)$ for cross-polarised pairs. $g^{(2)}(0)$ is the integrated number of events in the central peak. From these values the fidelity to the $\frac{1}{\sqrt{2}}(|H_{XX}H_X\rangle + |V_{XX}V_X\rangle)$ state can be calculated by $F = (1 + C_R + C_D - C_C)/4$. This fidelity value is readily accepted by the scientific community as an evaluation of

entanglement [16, 17]. It is also much quicker to measure the fidelity, which requires measurements in 3 bases, than to do a full photonic state tomography procedure, which requires 16 basis measurements [18].

2.4 Modelling the experiment.

The simulation[2, 3] attempts to realistically model the single photon correlation curves and polarization resolved correlation curves from a semiconductor quantum dot. A monte carlo simulation of the QD was combined with a model of the optical bench, this allows a monte carlo simulation of the experiment and of various results such as the polarisation resolved correlation curve or photonic state tomography [18].

Quantum dot Monte Carlo. This monte carlo model simulates the QD emission properties, namely, its emission probabilities related to the excitation laser or current and its emission time statistics. For the polarization resolved curves fine structure splitting and decoherence effects were also taken into account. The Poisson photon emission probability of the quantum dot after excitation by a laser or a voltage are [25]

$$p_x(n) = 1 - e^{-n} \quad (2.2)$$

$$p_{xx}(n) = 1 - (1 + n)e^{-n} \quad (2.3)$$

Where p_x and p_{xx} are the probabilities of exciton and biexciton emission respectively, n is the mean number of generated excitons in the bulk/vicinity of the dot. These are assumed, and will naturally give rise to the typical single and cross correlation curves in pulsed excitation mode.

The exciton and biexciton lifetimes are randomly chosen from an exponential decay with characteristic lifetime τ_x and τ_{xx} respectively. The characteristic lifetime of the biexciton is typically around half that of the exciton. It is made sure in the simulation that the specific biexciton emission lifetime is always shorter than that of the exciton.

In the polarization resolved case a biphoton state is emitted. This is represented by

$$|\psi\rangle = |H_x H_{xx}\rangle + e^{iFSS \tau/\hbar} |V_x V_{xx}\rangle \quad (2.4)$$

The phase term is given by $e^{iFSS \tau/\hbar}$ where FSS is the fine structure splitting and τ is the time between the biexciton and exciton emission. In the perfect case of no fine structure splitting the phase term will always be 1.

Decoherence must also be taken into account, this is a process whereby the phase term randomly shifts. Here it is phenomenologically categorised by a characteristic cross decoherence time of τ_{HV} . It is reported that this time τ_{HV} is typically[15] longer than the exciton lifetime, implying that QD excitons have a coherence $>70\%$, i.e. 70% of the time the emission will not have a random phase shift.

Modelling the optical bench. A model of the optical elements includes mathematically writing the photonic state in an algebraic lab basis and by using Jones tensor algebra[6, 8] the state can be propagated through the optical bench. The degrees of freedom in this basis are photonic polarization, direction and energy. Polarization is needed since the photons from the quantum dot should be polarization entangled. Direction is needed in order to tell the difference between the output paths of a polarising beam splitter (PBS) and a neutral beam splitter (NBS). Energy is needed to differentiate between the exciton and biexciton state.

The polarisation basis is given by[9]:

$$\hat{h} = \begin{pmatrix} 1 \\ 0 \end{pmatrix}, \hat{v} = \begin{pmatrix} 0 \\ 1 \end{pmatrix} \quad (2.5)$$

The direction basis is given by:

$$\hat{i} = \begin{pmatrix} 1 \\ 0 \end{pmatrix}, \hat{j} = \begin{pmatrix} 0 \\ 1 \end{pmatrix} \quad (2.6)$$

The energy basis is given by:

$$\hat{e}_x = \begin{pmatrix} 1 \\ 0 \end{pmatrix}, \hat{e}_{xx} = \begin{pmatrix} 0 \\ 1 \end{pmatrix} \quad (2.7)$$

For example, an input photon that is \hat{h} polarized, moving in the x direction and with energy \hat{e}_x is calculated by: $\gamma_{eg} = \hat{h} \otimes \hat{i} \otimes \hat{e}_x$, where \otimes is the tensor product operator.

These basis matrices are used to categorise matrix operators for various optical bench apparatus, namely the neutral and polarising beam splitters and monochromators. The matrix operators can be found by mapping each of the input states to the output states [6].

$$M = \sum_i |\text{in}_i\rangle \langle \text{out}_i| \quad (2.8)$$

The input and output states and matrix operators are presented in Appendix A for the neutral and polarising beam splitters and monochromators. For the wave plates, rotated at an angle θ to the optical axis, the common Jones matrices are used [10].

$$HWP = \begin{pmatrix} \cos 2\theta & \sin 2\theta \\ \sin 2\theta & -\cos 2\theta \end{pmatrix} \quad (2.9)$$

$$QWP = \begin{pmatrix} 1 + i \cos 2\theta & i \sin 2\theta \\ i \sin 2\theta & 1 - i \cos 2\theta \end{pmatrix} \quad (2.10)$$

These are then adapted to the lab basis. The adapted matrices derived for the PBS (polarising beam splitter), S (monochromator), NBS (neutral beam splitter), QWP and HWP are presented in Appendix A. The detector matrices are simply given by the photonic state that the detector is allowed measure, for example Detector1 in Figure 8 is only able to measure \hat{h} polarized photons with energy \hat{e} moving in the \hat{i} direction.

$$D1 = \hat{h} \otimes \hat{i} \otimes \hat{e}_x \quad (2.11)$$

$$D2 = \hat{v} \otimes \hat{i} \otimes \hat{e}_x \quad (2.12)$$

$$D3 = \hat{h} \otimes \hat{i} \otimes \hat{e}_{xx} \quad (2.13)$$

$$D4 = \hat{v} \otimes \hat{j} \otimes \hat{e}_{xx} \quad (2.14)$$

All of the matrices defined here act on a single photon state. In the entangled photon case each of this matrices are modified by the relation[11]

$$M_e = M \otimes M \quad (2.15)$$

The total optical bench operator is then given by

$$L_e = PBS_e \cdot S_e \cdot QWP_e \cdot HWP_e \cdot NBS_e \quad (2.16)$$

The detector pair matrices are given by

$$D_i D_j = D_i \otimes D_j \quad (2.17)$$

The pairs D1D3, D1D4, D2D3, D2D4 are always used. We can then find what the probability of a given input state $|\psi\rangle$ will have of hitting a detector pair $D1D3$ is given by

$$P_{D1D3} = |D1D3^T \cdot L_e \cdot |\psi\rangle|^2 \quad (2.18)$$

The simulation algorithm The simulation starts by generating the photonic state $|\psi\rangle = |H_x H_{xx}\rangle + e^{iS\tau/\hbar} |V_x V_{xx}\rangle$ in the lab basis

$$|\psi\rangle = \left| (\hat{h} \otimes \hat{i} \otimes \hat{e}_x) \otimes (\hat{h} \otimes \hat{i} \otimes \hat{e}_{xx}) \right\rangle + e^{iS\tau/\hbar} \left| (\hat{v} \otimes \hat{i} \otimes \hat{e}_x) \otimes (\hat{v} \otimes \hat{i} \otimes \hat{e}_{xx}) \right\rangle \quad (2.19)$$

The lifetime is generated and the phase calculated, if a decoherence event happens before the lifetime is finished, the phase is shifted by some random amount. The state is then operated on by the lab matrix and the detector pair probabilities are calculated. Then stochastically, a single detector, or pair of detectors were chosen according to these probabilities. Tagging each detector with a hit time according to the lifetime and laser pulse interval of the exciton or biexciton the polarisation resolved correlation curves are generated. These curves can be generated in different polarisation bases by changing the waveplate angles.

3 Time resolved entanglement

The theoretical and experimental work to validate the idea of time dependent entanglement is discussed in this chapter. This work was done by the author and Dr. Gediminas Juska, both took measurements and both worked on the processing.

3.1 Theory of time gating.

As explained in Chapter 1 the entangled photonic state from the QD is predicted to be[14]:

$$|\psi\rangle = \frac{1}{\sqrt{2}} \left(|H_{XX}H_X\rangle + e^{\frac{iFSS}{\hbar} \tau_{\Delta}} |V_{XX}V_X\rangle \right). \quad (3.1)$$

Where τ_{Δ} is the time between biexciton and exciton photon emission and FSS is the exciton fine structure splitting. If the FSS is large enough this phase oscillation becomes fast and when averaged over all QD emissions with τ_{Δ} obeying an exponential distribution, the phase will average out to zero. The state is still entangled, however each emitted pair is different and under measurement will seem to be classical light.

Since it is not feasible to change the FSS of each emission, we instead discriminate the data based on τ_{Δ} . We choose only small τ_{Δ} in the correlation curves by applying a time gate. This time gate is shown schematically in Figure 9.

Consider a gate that starts at time t_0 and has a width Δt . For $t_0 = 0$ and $\Delta t \rightarrow 0$ we would expect the maximally entangled state

$$|\psi\rangle = \frac{1}{\sqrt{2}} (|H_{XX}H_X\rangle + |V_{XX}V_X\rangle). \quad (3.2)$$

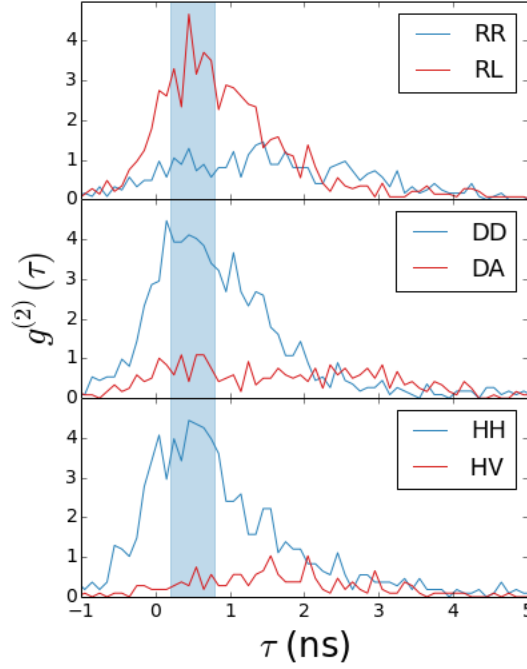


Figure 9: A simple gate applied to the central peak of the correlation curve shown in Figure 10.

Decoherence[15] will reduce the measurable fidelity to this state to some value $F_{max} \leq 1$. In practice the gate must have some nonzero finite width. If t_0 is kept constant and the Δt is increase it would be expected that the fidelity will drop as photon pairs with a different τ_Δ are included in the calculation. The biphoton intensity will increase for larger τ_Δ . If Δt is kept constant and t_0 is increased it would be expected that the fidelity will vary sinusoidally synchronised with the state phase. If the measured fidelity is plotted versus the gate start time for an adequately small Δt it should be possible to derive an accurate estimation of the FSS.

In theory by choosing vanishingly small Δt it would be possible to prepare an entangled state with every conceivable phase. In practice however since the biexciton and exciton lifetimes are exponentially decreasing, the emission intensity is exponentially decreasing as t_0 increases.

3.2 Experimental data.

In Figure 10 is shown the measured correlation curves in linear, diagonal and circular bases. In this measurement the time resolution was 0.1 ns which is considered to be high enough for time gating.

The degree of correlation in each basis can be calculated by [17]:

$$C = \frac{g_{\parallel}^{(2)}(0) - g_{\perp}^{(2)}(0)}{g_{\parallel}^{(2)}(0) + g_{\perp}^{(2)}(0)} \quad (3.3)$$

Where $g_{\parallel}^{(2)}(\tau)$ is the $g^{(2)}$ value for co-polarised pairs and $g_{\perp}^{(2)}(\tau)$ for cross-polarised pairs. $g^{(2)}(0)$ is the integrated number of events in the central peak.

The degree of correlation in linear, diagonal and circular polarisation bases were calculated to be $C_R = 0.66 \pm 0.06$, $C_D = 0.46 \pm 0.04$, $C_C = -0.31 \pm 0.02$ respectively.

From these values the fidelity to the $\frac{1}{\sqrt{2}}(|H_{XX}H_X\rangle + |V_{XX}V_X\rangle)$ state can be calculated by :

$$F = \frac{1 + C_R + C_D - C_C}{4}. \quad (3.4)$$

The value calculated was $F = 0.61 \pm 0.02$. The errors in the degree of correlations and the fidelity were calculated by taking the standard deviation of the same result in the side peaks. The side peaks should have $C = 0$, and any fluctuations would be due to noise, this noise was taken to be the error in the results.

The fidelity limit for classical light is 0.5, the fidelity calculated from the data beats this limit by over 5 standard deviations. Clearly the photons emitted from the quantum dot are exhibiting quantum behaviour.

When the phase of the photonic state is included into the discussion it is understood that this fidelity value is the average of all the events with gate $t_0 \rightarrow -\alpha$ and $\Delta t \rightarrow \alpha$ where α is half the time between laser pulses, $\alpha = 6.25ns$ in the case presented here.

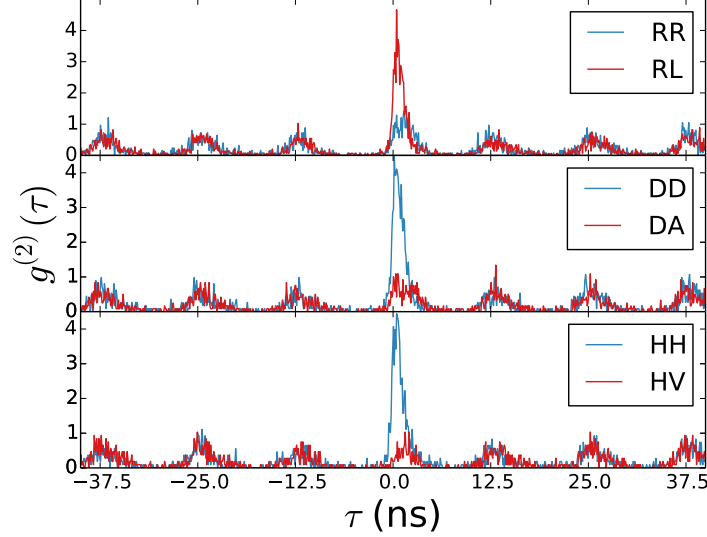


Figure 10: Measured correlation curves in the linear, diagonal and circular bases.

3.2.1 Fidelity versus gate start time.

Figure 11 presents the results when a gate was applied to the correlation curves from Figure 10. First a gate was applied with $\Delta t = 0.2ns$ and $t_0 = -2 \rightarrow 6ns$ ($\delta t = 0.2ns$). Figure 11 (a) clearly shows a sinusoidal dependence of the fidelity on t_0 . The error in the data was again calculated using the side peaks.

The FSS can be calculated from the curve by fitting a sinusoid and calculating the frequency. The angular frequency of the fit is $\nu_f \pm \Delta\nu_f$. We want the term $e^{\frac{iS\tau\Delta}{\hbar}}$ to oscillate with period 2π , where $\nu = \frac{1}{\tau_\Delta}$. The result after substitution is:

$$S = \hbar\nu_f \quad (3.5)$$

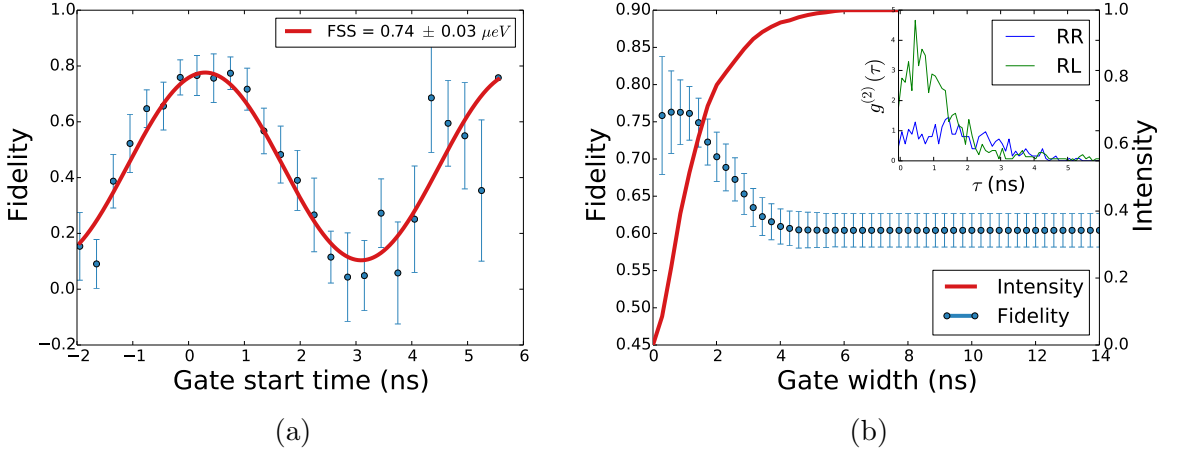


Figure 11: (a) Measured fidelity vs gate start for a gate width of 0.2 ns (b) Measured fidelity vs gate width starting at 0 ns , the inset shows the section of the curve used.

The resulting FSS is calculated to be $0.74 \pm 0.03 \mu\text{eV}$. In Figure 11 (a) it is seen that the fidelity can rise to almost 0.8 and drop to less than 0.2, this low value implies increased fidelity to the state:

$$|\psi\rangle = \frac{1}{\sqrt{2}} (|H_{XX}H_X\rangle - |V_{XX}V_X\rangle). \quad (3.6)$$

However there is not enough intensity within this gate to conclusively show correlation curves for this state. A QD with FSS of around $0.2 \sim 0.3 \mu\text{eV}$ might be better suiting to preparing this state because the phase oscillations would be slower. However anytime this state is prepared, it comes at a cost of much reduced intensity.

3.2.2 Fidelity versus gate width.

Figure 11 (b) presents the curve obtained when a gate was applied to the data with $t_0 = 0 \text{ ns}$ and Δt was varied. It is seen that when Δt is small the fidelity is higher, hitting a high of fidelity of 0.75. As Δt is increased, longer time phase events are included and the fidelity is expected to drop, this is what we observe. As the gate is opened even more the fidelity drops to a constant value matching the average fidelity

calculated earlier of $F = 0.61 \pm 0.02$.

It should be pointed out however is the QD's measured in this work, when a gate is applied that retains 70% of the intensity a rise in fidelity from 0.61 to 0.75 can be observed. This would be quite useful in the future if a physical shutter time gate was used.

The slight plateau in the fidelity at very small values of Δt is attributed to the rise time in the correlation curves near $t_0 = 0ns$.

3.3 Simulation results.

The experimental results presented above were also compared with theoretical results presented in this section. Using the Monte Carlo simulation explained in the Chapter 2, the correlation curves were generated and the time gate processing was applied.

Figure 12 and Figure 13 show these simulated results. Overall there is very good agreement between the simulations and data.

Parameter	Value
Exciton lifetime	2 ns
Biexciton lifetime	1 ns
Mean excitons in vicinity per pulse	1
FSS	$0.7 \mu eV$
Decoherence time	10^6 ns
Background rate	15%
Detector response	0.3 ns

Table 1: Parameters used to simulate the curves in Figure 12 and Figure 13.

The simulation takes into account decoherence events, detector response, FSS, lifetimes, emission intensity and background emission. Many of these parameters are measurable directly, (FSS, lifetimes, intensity, detector response) some cannot be measured directly (background and decoherence). A useful curve that the simulation

can predict is the fidelity versus FSS, which has been shown to be a Lorentzian [15], however tuning the FSS to measure this curve was outside the scope of this work.

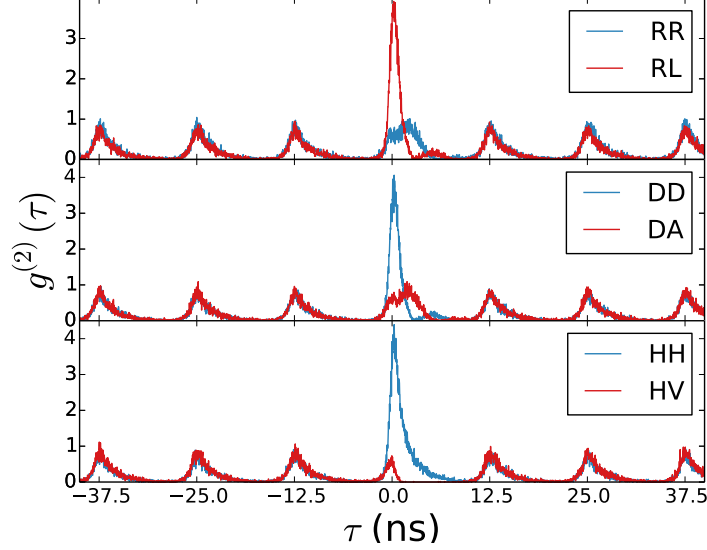


Figure 12: Monte Carlo simulated correlation curves in the linear, diagonal and circular bases.

The simulation is able to recreate results for single photon exciton-exciton auto correlation curves and exciton-biexciton correlation curves. Presented here are the polarization resolved biexciton-exciton curves. The parameters used are presented in Table 1. A large decoherence time was chosen such that the probability of a decoherence event occurring in the simulation was effectively zero. This was done to clearly show the time dependence in the correlation curves.

The data from the simulated correlation curves was treated in the exact same way as the measured correlation curves when time gated. Figure 13 shows the simulated fidelity versus gate start time and gate width. They are in very good agreement with the measured results.

This theory of time dependent entanglement is supported by the data presented in this chapter. It is important to understand this time dependent entanglement when designing QD's, it gives a quantitative measure on how the FSS and the exciton, biex-

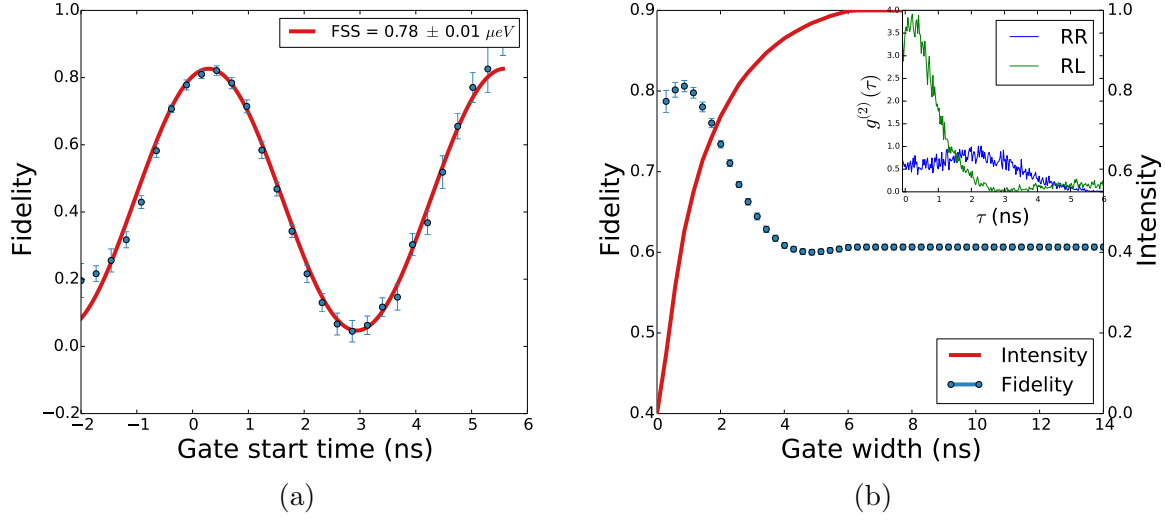


Figure 13: (a) Monte Carlo simulated fidelity vs gate start for a gate width of 0.2 ns (b) Monte Carlo simulated fidelity vs gate width starting at 0 ns .

citon lifetimes will influence measured entanglement. Making the FSS and lifetimes smaller is the preferable approach.

This theory could potentially be used to allow fine control of the phase of the emitted photonic state. Pre-selection in time of the emitted photons would be quite useful as opposed to the post-selection presented in this work. This phase selection comes at a cost of intensity, however this may be compensated by having suitably efficient collection.

4 Charged biexciton states

This chapter concerns the identification of a specific excitonic pattern present in the QDs emitting entangled photons. This work was done by the author and Dr. Gediminas Juska, both took measurements, while Dr. Juska developed the theory and the author worked on the mathematical modeling.

4.1 Theory

A constant feature of the QDs reported by the EPN group in Ref [5] and presented in Chapter 3 of this work is a typical spectrum for the entangled photon emitting QD's. It is seen that there is two distinct spectrum on the sample. One of which consistently ($\sim 75\%$) passes entanglement tests, and one which always fails. In this chapter a detailed analysis was done on the entangled photon emitting pattern, shown in Figure 14. As will be discussed, it is hypothesised that the population of these QDs is dominated by positively charged carriers. A describing fine structure is tentatively presented and then data and models are presented to reinforce the theory [1].

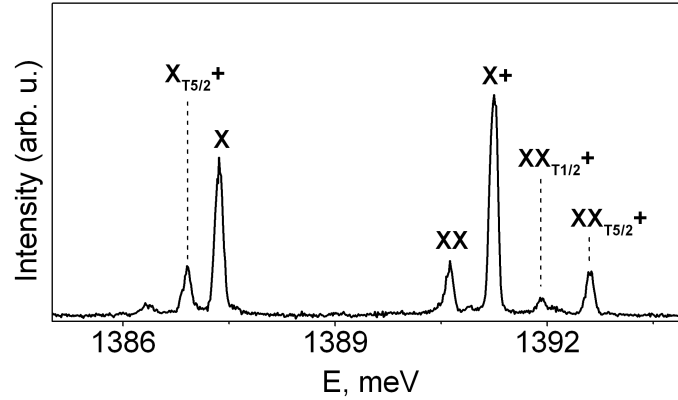


Figure 14: Typical spectrum of QDs which pass entanglement tests. ³

A trion is an exciton which has a surplus electron or hole, a hot trion is when the surplus carrier is in the excited state. It is assumed that this charged environment is

³Courtesy of Dr. Juska

an independent product of whatever growth process creates these highly symmetric QDs and that the pattern is not in itself an inherent properties highly symmetric dots. Unambiguous identification of whether the excitonic species was positively or negatively charged was not made in the scope of this work. A QD light-emitting diode structure [20] is a strategy for identification of whether the QD charging is positive or negative. This LED structure is under preliminary development for pyramidal QDs and was unavailable at this time. Thus the identification of the charging environment as positive is based on equivalence with literature (Review. [19]). Theoretically there is no limit on the energetic structure of different charging configurations however it is typically reported that positive QDs are at higher energy than neutral, and the negative QDs are at lower energy.

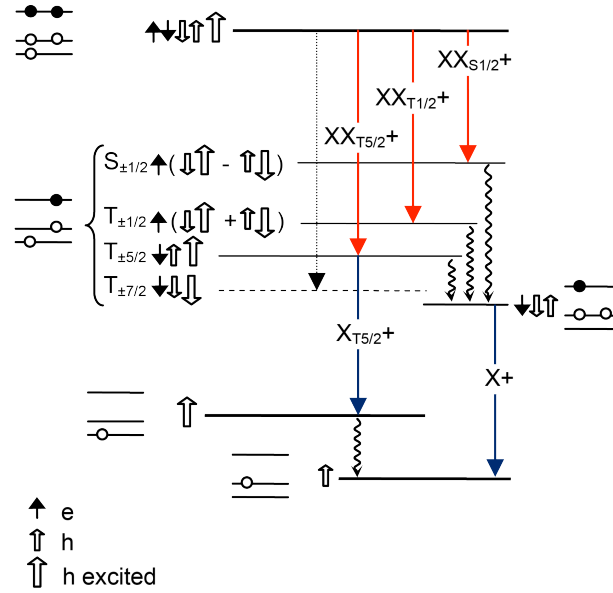


Figure 15: Energetic structure of the biexciton ⁴

The theorised fine structure of charged biexciton system is depicted in Figure 15 [21, 22, 23]. The recombination from the initial charged biexciton state is complicated by the fine-structure of the hot trion. According to Kramers theorem, an energy level with half-integer spin is at least doubly degenerate, the initial charged biexciton state ($\pm 3/2$) is double degenerate. It decays to a hot trion, one electron and two

⁴Courtesy of Dr. Juska

holes – one ground hole and the other excited. The hot trion has eight possible total spin configurations resulting in eightfold degeneracy. The hole-hole exchange interaction causes the splitting of the energetic level to a double degenerate singlet state ($\pm 1/2$) and a six-fold triplet state. Electron-hole exchange interaction causes a further splitting of the triplet states. The resulting energy fine-structure has four double degenerate levels [22]. The singlet state $S_{\pm 1/2}$ is the highest energy state followed by $T_{\pm 1/2}$, $T_{\pm 5/2}$ and $T_{\pm 7/2}$.

Identification of the transitions was carried out by excitation power dependent and photon cross-correlations measurements and a theoretical QD population model. The typical spectrum shown in Figure 14 was made up of transitions that originated from two recombination cascades – the neutral biexciton-exciton cascade and that of the positively charged biexciton-excited trion. A populated charged biexciton decays optically to the three doubly degenerate hot trion states. These transitions are observed as $XX_{S1/2+}$, $XX_{T1/2+}$ and $XX_{T5/2+}$ in the spectrum. Transition to the $T_{\pm 7/2}$ state is forbidden by optical recombination. The singlet $S_{\pm 1/2}$ and the triplet $T_{\pm 1/2}$ states are believed to be very short living and decay to the ground trion as the excited hole very rapidly relaxes to the ground level [22, 23]. The state $T_{\pm 5/2}$ is composed of a ground hole and excited hole that have the same spin, thus the excited hole relaxation to the ground level is restricted by Pauli exclusion principle. If the hole spin flip rate γ_{sf} is comparable to the spontaneous recombination rate then this state can recombine optically, this is transition $X_{T5/2+}$ in the spectrum.

4.2 Experimental and modelling

Photon correlation measurements taken in a continuous-wave excitation mode allowed the identification of the cascade order of the transitions. These measured second order correlation $g^{(2)}(\tau)$ curves are shown in Figure 16. On the positive time scale the second order correlation function represents the probability of detecting a photon emitted by transition T_n being followed by a photon emitted by a transition T_m . On

the negative timescale the opposite is true (T_m being followed by T_n). For example there should be an increased probability of an XX photon being followed by an X photon and decreased probability of the reverse occurring (Top image in Figure 16).

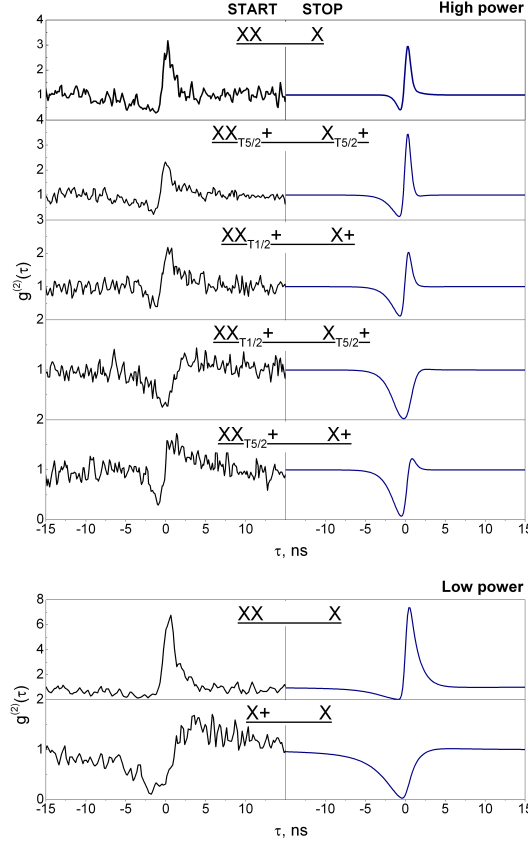


Figure 16: Measured and theoretical correlations curves for different transition pairs.

A rate equation model was developed to analyse the correlation curves. This model was based on the theory of random population presented in Ref [25] and charged excitonic model in Ref [24]. The model presented here includes also excited excited states (and excludes negative states). The probability of being in a given state $p_{it}(t)$ depends on the rates at which one enters and exits the state. A state is populated by capturing electrons and holes with characteristic times t_e and t_h , or by decaying into the state $p_{it}(t)$ from a transition cascade. A state exits by decaying optically with characteristic lifetime τ_{ij} or by moving to another state by electron or hole capture.

In general the rate of change of the state probability is given by

$$\frac{d\bar{P}}{dt} = A\bar{P} \quad (4.1)$$

Where A is a transition matrix made up of the rate of entering and exiting a state.

The rate equations are presented here

$$\frac{dp_{000}}{dt} = \frac{p_{101}}{\tau_{101}} - \frac{p_{000}}{t_h} - \frac{p_{000}}{t_e}, \quad (4.2)$$

$$\frac{dp_{100}}{dt} = \frac{p_{000}}{t_h} + \frac{p_{201}}{\tau_{201}} - p_{100}\frac{c_e}{t_e} - p_{100}\frac{c_h}{t_h} + \frac{p_{010}}{\tau_{010}}, \quad (4.3)$$

$$\frac{dp_{200}}{dt} = p_{100}\frac{c_h}{t_h} - p_{200}\frac{c_e}{t_e}, \quad (4.4)$$

$$\frac{dp_{001}}{dt} = \frac{p_{000}}{t_e} - p_{001}\frac{d_h}{t_h}, \quad (4.5)$$

$$\frac{dp_{010}}{dt} = \frac{p_{111}}{\tau_{111}} - \frac{p_{010}}{\tau_{010}}, \quad (4.6)$$

$$\frac{dp_{101}}{dt} = p_{100}\frac{c_e}{t_e} + p_{001}\frac{d_h}{t_h} + \frac{p_{202}}{\tau_{202}} - \frac{p_{101}}{\tau_{101}} - \frac{p_{101}}{t_h}, \quad (4.7)$$

$$\frac{dp_{111}}{dt} = \frac{2}{3}\frac{p_{212}}{\tau_{212T5/2}} + \frac{1}{2}\frac{p_{101}}{t_h} - \gamma_{sf}p_{111} - \frac{p_{111}}{\tau_{111}}, \quad (4.8)$$

$$\frac{dp_{201}}{dt} = \frac{1}{2}\frac{p_{101}}{t_h} + p_{200}\frac{c_e}{t_e} + \frac{1}{3}\frac{p_{212}}{\tau_{212T1/2}} + \gamma_{sf}p_{111} - p_{201}\frac{c_e}{t_e} + \frac{p_{201}}{\tau_{201}}, \quad (4.9)$$

$$\frac{dp_{202}}{dt} = p_{201}\frac{c_e}{t_e} - \frac{p_{202}}{\tau_{202}} - \frac{p_{202}}{t_h}, \quad (4.10)$$

$$\frac{dp_{212}}{dt} = \frac{p_{202}}{t_h} - \frac{1}{3}\frac{p_{212}}{\tau_{212T1/2}} - \frac{2}{3}\frac{p_{212}}{\tau_{212T5/2}}, \quad (4.11)$$

$$\sum_i p_i(t) = 1 \quad (4.12)$$

Where p_{abc} is the probability of being in state with a holes, b excited holes and c

electrons. τ_{abc} is the decay time of state with a holes, b excited holes and c electrons. Where γ_{sf} is the excited hole spin flip time. t_e (t_h) is the electron (hole) capture time and c_e , c_h , d_e , d_h are Coulomb coefficients as explained below. These equations are represented schematically in Figure 17. Red arrows represent radiative recombination and the measurable emission of a photon. The radiative lifetimes τ_{ij} were measured and used directly in the modeling.

A $g^{(2)}(\tau)$ curve was modeled by plotting on the positive timescale $p_i(t)$ which decays to state $p_j(t)$ with the initial condition of being in whatever state populates state i , and $p_j(t)$ with initial condition of being in the state j on the negative timescale.

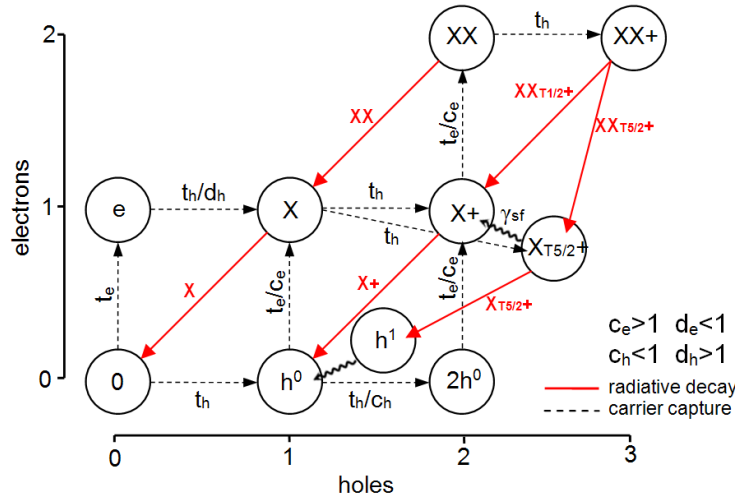


Figure 17: Schematic of the rate equations used model the measured correlations.

The response function of the APDs was measured to be a Gaussian and has a FWHM of 0.71ns. The model accounted for this by numerically convoluting the rate equations with this response function. Coulomb interactions were included in the model. These interactions occur when the QD is populated by a charged complexes, for example electron capture is faster when the QD is positively charged. The corrections modify the electron (hole) capture time t_e (t_h) reducing (increasing) it by c_e (c_h) when a QD is positively charged and increasing (reducing) it by d_e (d_h) when charging is negative. Since the QD is negatively charged in only one instance, when it is populated by an

electron, the term d_e never comes into play and d_h is included only didactically. The following simplifications were made in the model. In the spectrum shown in Figure 14, only the two transitions $XX_{T1/2+}$ and $XX_{T5/2+}$ from the charged biexciton to the triplet states were clearly observed. The relaxation of the hot trion state $X_{T1/2+}$ to the ground trion X_+ is reported to be very rapid [23], on the order of picoseconds which is ignored on the scale of the model which is nanoseconds. Thus in the model the state $X_{T1/2+}$ was considered equivalent to the state X_+ . The state $X_{T5/2+}$ needs a spin flip in order to decay to X_+ . Thus it lives longer. A hole spin flip term γ_{sf} was included in the state $X_{T/2+}$ equation, similarly to Ref. [23].

The fitting to the experimental data was done quite strictly with the only free parameters being the coulomb terms c_e and c_h , the electron and hole capture times t_e and t_h , the hole relaxation time τ_{001} and the spin flip time γ_{sf} . This is in contrast to similar models where the radiative lifetimes are not set parameters. The small discrepancies between the model and experiment can be explained by the complexity of the system and the measurement procedure. The fittings assume that the parameters are constant throughout the whole measurement, which is unlikely in practice as the experiment typically takes a few hours. Sample drifting and power fluctuations would have the effect of slightly modifying the measurement conditions over time. There is a good overall agreement between the fittings and the data, especially since the same model was used to describe the high and low power measurements. The spin flip time γ_{sf} of the excited hole was calculated to be 1.8ns^{-1} (0.55ns) which is of the same scale as the radiative lifetime of the $X_{T5/2+}$ state. The electron capture time t_e was found to be 1.03ns and the hole capture time t_h was found to be 0.38ns. This smaller hole capture time is consistent with the positively dominated excitonic system.

5 Conclusions and further work

This report has been a summary of work done to categorise and fully understand the entangled photon emitting QDs.

Chapter 3 was concerned with understanding the time evolution of the polarisation entanglement. Using the time gating theory a dramatic rise in the entanglement fidelity was achieved. This theory is important both for understanding the underlying dynamics of the biexciton-exciton entangled cascade and also as a technique to achieve higher fidelity in a regime where time discrimination is possible. There may also be use cases in time-dependent quantum logic, where the phase of the entangled state may be chosen.

Chapter 4 presented a detailed study on the excitonic pattern observed in the QDs which have a high propensity for entangled photon emission. A theoretical model was developed and was seen to have good agreement with the measurements. Further work has been done in this area by the group since the end of this project. It has been seen that the second excitonic patterns seen on the sample are likely to be negatively charged. This implies that the entangled photon emission from the second pattern may only be practically useless, because the exciton intensity is so low. This negative charging has the ability to be tuned by adding a second excitation wavelength (around $1\ \mu\text{m}$) which allowed gradual tuning of the QD from positive to negative. This tuning has the potential to greatly increase the density of entangled photon emitters.

Further work would include investigating the QDs under resonant excitation, where the exciton and biexciton states are populated directly. With this neutral excitation the quality of the spectrum and the entanglement may improve. The group is also now focusing on different tuning strategies for the QDs. QDs integrated on piezoelectric crystals can be tuned through strain has been shown by the group to alter the wavelength through a few meV. The FSS has been shown to be tunable by a vertical electric field [26].

6 Appendix 1

The HWP matrix adapted to the lab basis is give by:

$$HWP = \begin{pmatrix} hwp(\theta_x) & 0 & 0 & 0 & 0 & 0 & 0 \\ & 0 & 0 & 0 & 0 & 0 & 0 \\ 0 & 0 & hwp(\theta_x) & 0 & 0 & 0 & 0 \\ 0 & 0 & & 0 & 0 & 0 & 0 \\ 0 & 0 & 0 & 0 & hwp(\theta_{xx}) & 0 & 0 \\ 0 & 0 & 0 & 0 & & 0 & 0 \\ 0 & 0 & 0 & 0 & 0 & 0 & hwp(\theta_{xx}) \\ 0 & 0 & 0 & 0 & 0 & 0 & 0 \end{pmatrix}$$

Where hwp is

$$hwp = \begin{pmatrix} \cos 2\theta & \sin 2\theta \\ \sin 2\theta & -\cos 2\theta \end{pmatrix}$$

The QWP matrix adapted to the lab basis is give by:

$$QWP = \begin{pmatrix} qwp(\theta_x) & 0 & 0 & 0 & 0 & 0 & 0 \\ & 0 & 0 & 0 & 0 & 0 & 0 \\ 0 & 0 & qwp(\theta_x) & 0 & 0 & 0 & 0 \\ 0 & 0 & & 0 & 0 & 0 & 0 \\ 0 & 0 & 0 & 0 & qwp(\theta_{xx}) & 0 & 0 \\ 0 & 0 & 0 & 0 & & 0 & 0 \\ 0 & 0 & 0 & 0 & 0 & 0 & qwp(\theta_{xx}) \\ 0 & 0 & 0 & 0 & 0 & 0 & 0 \end{pmatrix}$$

Where qwp is

$$qwp = \begin{pmatrix} 1 + i \cos 2\theta & i \sin 2\theta \\ i \sin 2\theta & 1 - i \cos 2\theta \end{pmatrix}$$

Here we present the mappings made for the optical bench apparatus.

For the neutral beam splitter (NBS) this operator is given by making the mapping:

$$\begin{aligned} NBS \left| \psi^{\hat{i}} \right\rangle &= \frac{1}{\sqrt{2}} (\left| \psi^{\hat{i}} \right\rangle + \left| \psi^{\hat{j}} \right\rangle) \\ NBS \left| \psi^{\hat{j}} \right\rangle &= \frac{1}{\sqrt{2}} (\left| \psi^{\hat{i}} \right\rangle + \left| \psi^{\hat{j}} \right\rangle) \end{aligned}$$

Where $\left| \psi^{\hat{i}} \right\rangle$ is a state moving in the \hat{i} direction. With matrix

$$NBS = \frac{1}{\sqrt{2}} \begin{pmatrix} 1 & 0 & 1 & 0 & 0 & 0 & 0 & 0 \\ 0 & 1 & 0 & 1 & 0 & 0 & 0 & 0 \\ 1 & 0 & 1 & 0 & 0 & 0 & 0 & 0 \\ 0 & 1 & 0 & 1 & 0 & 0 & 0 & 0 \\ 0 & 0 & 0 & 0 & 1 & 0 & 1 & 0 \\ 0 & 0 & 0 & 0 & 0 & 1 & 0 & 1 \\ 0 & 0 & 0 & 0 & 1 & 0 & 1 & 0 \\ 0 & 0 & 0 & 0 & 0 & 1 & 0 & 1 \end{pmatrix}$$

In general beam splitters impart a phase rotation on the reflected state, however a phase difference in the positional degree of freedom is not measured in the simulation. It was tested and seen to not make any difference in the results of the simulation. The polarising beam splitter (PBS) is given by making the mappings:

$$PBS \left| \hat{i} \hat{h} \hat{e}_{xx} \right\rangle = \left| \hat{i} \hat{h} \hat{e}_{xx} \right\rangle$$

$$PBS \left| \hat{i} \hat{v} \hat{e}_{xx} \right\rangle = \left| \hat{j} \hat{h} \hat{e}_{xx} \right\rangle$$

$$PBS \left| \hat{i} \hat{h} \hat{e}_x \right\rangle = \left| \hat{i} \hat{h} \hat{e}_x \right\rangle$$

$$PBS \left| \hat{i} \hat{v} \hat{e}_x \right\rangle = \left| \hat{j} \hat{h} \hat{e}_x \right\rangle$$

$$PBS \left| \hat{j} \hat{h} \hat{e}_{xx} \right\rangle = \left| \hat{j} \hat{h} \hat{e}_{xx} \right\rangle$$

$$PBS \left| \hat{j} \hat{v} \hat{e}_{xx} \right\rangle = \left| \hat{i} \hat{h} \hat{e}_{xx} \right\rangle$$

$$PBS \left| \hat{j} \hat{h} \hat{e}_x \right\rangle = \left| \hat{j} \hat{h} \hat{e}_x \right\rangle$$

$$PBS \left| \hat{j} \hat{v} \hat{e}_x \right\rangle = \left| \hat{i} \hat{h} \hat{e}_x \right\rangle$$

With matrix

$$PBS = \begin{pmatrix} 1 & 0 & 0 & 0 & 0 & 0 & 0 & 0 \\ 0 & 0 & 0 & 1 & 0 & 0 & 0 & 0 \\ 0 & 0 & 1 & 0 & 0 & 0 & 0 & 0 \\ 0 & 1 & 0 & 0 & 0 & 0 & 0 & 0 \\ 0 & 0 & 0 & 0 & 1 & 0 & 0 & 0 \\ 0 & 0 & 0 & 0 & 0 & 0 & 0 & 1 \\ 0 & 0 & 0 & 0 & 0 & 0 & 1 & 0 \\ 0 & 0 & 0 & 0 & 0 & 1 & 0 & 0 \end{pmatrix}$$

The \hat{e}_x monochromator (S_x) workes by only allowing energy \hat{e}_x through and is given by making the mappings:

$$S_x \left| \hat{i} \hat{h} \hat{e}_{xx} \right\rangle = \left| \hat{i} \hat{h} \hat{e}_{xx} \right\rangle$$

$$S_x \left| \hat{i} \hat{v} \hat{e}_{xx} \right\rangle = \left| \hat{i} \hat{h} \hat{e}_{xx} \right\rangle$$

$$S_x \left| \hat{i} \hat{h} \hat{e}_x \right\rangle = |0\rangle$$

$$S_x \left| \hat{i} \hat{v} \hat{e}_x \right\rangle = |0\rangle$$

The \hat{e}_{xx} monochromator (S_{xx}) workes by only allowing energy \hat{e}_{xx} through and is given by making the mappings:

$$S_{xx} \left| \hat{j} \hat{h} \hat{e}_{xx} \right\rangle = |0\rangle$$

$$S_{xx} \left| \hat{j} \hat{v} \hat{e}_{xx} \right\rangle = |0\rangle$$

$$S_{xx} \left| \hat{j} \hat{h} \hat{e}_x \right\rangle = \left| \hat{j} \hat{h} \hat{e}_x \right\rangle$$

$$S_{xx} \left| \hat{j} \hat{v} \hat{e}_x \right\rangle = \left| \hat{j} \hat{h} \hat{e}_x \right\rangle$$

The monochromator matrix S is given by the sum of S_x and S_{xx} .

$$S = \begin{pmatrix} 0 & 0 & 0 & 0 & 0 & 0 & 0 & 0 \\ 0 & 0 & 0 & 0 & 0 & 0 & 0 & 0 \\ 0 & 0 & 1 & 0 & 0 & 0 & 0 & 0 \\ 0 & 0 & 0 & 1 & 0 & 0 & 0 & 0 \\ 0 & 0 & 0 & 0 & 1 & 0 & 0 & 0 \\ 0 & 0 & 0 & 0 & 0 & 1 & 0 & 0 \\ 0 & 0 & 0 & 0 & 0 & 0 & 0 & 0 \\ 0 & 0 & 0 & 0 & 0 & 0 & 0 & 0 \end{pmatrix}$$

References

- [1] G. Juska, **E. Murray**, V. Dimastrodonato, T. H. Chung, A. Gocalinska & E. Pelucchi *Entangled photon emission from (111)B site-controlled Pyramidal quantum dots*. Submitted to Phys. Rev. B. (2014).
- [2] **E. Murray**, G. Juska, & E. Pelucchi *Monte Carlo simulation suite for various Quantum dot experiments* (In production).
- [3] **E. Murray**, <http://www.github.com/eoinmurray/icarus2> Accessed on 3rd April 2014.
- [4] Oliver Benson, Charles Santori, Matthew Pelton, & Yoshihisa Yamamoto. *Regulated and Entangled Photons from a Single Quantum Dot*. Phys. Rev. Lett. 84, 2513 (2000).
- [5] G. Juska, V. Dimastrodonato, L. O. Mereni, A. Gocalinska & E. Pelucchi. *Towards quantum-dot arrays of entangled photon emitters*. Nature Photonics 7, 527–531 (2013).
- [6] M. A. Nielsen & I. L. Chuang. *Quantum Computation and Quantum Information. Chapter 2*. Cambridge University Press (2000).
- [7] M. Fox *Quantum Optics, an introduction. Chapter 6*. Oxford University Press (2006).
- [8] R. C. Jones. *A new calculus for the treatment of optical systems, I. Description and Discussion of the Calculus*. Jour. Optical Society of America, 31, (7) 488–493 (1941).
- [9] G. Fowles. *Introduction to Modern Optics (2nd ed.)*. Dover (1989), p. 35.
- [10] A. Gerald & J. M. Burch. *Introduction to Matrix Methods in Optics (1st ed.)*. John Wiley & Sons. (1975)

- [11] F. Rioux <http://www.users.csbsju.edu/~textasciitildefrioux/photon/MZ-Polarization.pdf> Accessed on 3rd April 2014.
- [12] R. M. Stevenson, R. J. Young, P. See, D. G. Gevaux, K. Cooper, P. Atkinson, I. Farrer, D. A. Ritchie & A. J. Shields. *Magnetic field induced reduction of fine structure splitting in quantum dots*. Phys. Rev. B 73, 033306 (2006).
- [13] R. J. Young, R. M. Stevenson, A. J. Shields, P. Atkinson, K. Cooper, D. A. Ritchie, K. M. Groom, A. I. Tartakovskii, & M. S. Skolnick. *Inversion of the exciton fine structure splitting in quantum dots*. Physica E 32, 97 (2006)
- [14] R. Mark Stevenson, Andrew J. Hudson, Anthony J. Bennett, Robert J. Young, Christine A. Nicoll, David A. Ritchie, Andrew J. Shields. *Evolution of Entanglement Between Distinguishable Light States*. Phys. Rev. Lett. 101, 170501 (2008).
- [15] A. J. Hudson, R. M. Stevenson, A. J. Bennett, R. J. Young, C. A. Nicoll, P. Atkinson, K. Cooper, D. A. Ritchie, & A. J. Shields. *Coherence of an entangled exciton-photon state*. Phys. Rev. Lett. 99, 266802 (2007).
- [16] M. Ghali, K. Ohtani, Y. Ohno & H. Ohno. *Generation and control of polarization-entangled photons from GaAs island quantum dots by an electric field*. Nat. Commun. 3, 661 (2012).
- [17] R. M. Stevenson, C. L. Salter, J. Nilsson, A. J. Bennett, M. B. Ward, I. Farrer, D. A. Ritchie, & A. J. Shields *Indistinguishable Entangled Photons Generated by a Light- Emitting Diode*. Phys. Rev. Lett. 108, 040503 (2012).
- [18] D. F. V. James, P. G. Kwiat, W. J. Munro, and A. G. White *Measurement of qubits*. Phys. Rev. A 64, 052312 (2001).
- [19] A. Schliwa, M. Winkelkemper, & D. Bimberg. *Few-particle energies versus geometry and composition of $In_xGa_{1-x}As$ /GaAs self-organized quantum dots* Phys. Rev. B 79, 075443 (2009).

- [20] M. Baier, F. Findeis, A. Zrenner, M. Bichler, & G. Abstreiter. *Optical spectroscopy of charged excitons in single quantum dot photodiodes*. Phys. Rev. B 64, 195326 (2001).
- [21] E. Poem, J. Shemesh, I. Marderfeld, D. Galushko, N. Akopian, D. Gershoni, B. D. Gerardot, A. Badolato, & P. M. Petroff. *Polarization sensitive spectroscopy of charged quantum dots*. Phys. Rev. B 76, 235304 (2007).
- [22] T. Warming, E. Siebert, A. Schliwa, E. Stock, R. Zimmermann, & D. Bimberg. *Hole-hole and electron-hole exchange interactions in single InAs/GaAs quantum dots*. Phys. Rev. B 79, 125316 (2009).
- [23] Y. Igarashi, et al. *Spin dynamics of excited trion states in a single InAs quantum dot*. Phys. Rev. B 81, 245304 (2010).
- [24] M. H. Baier, A. Malko, E. Pelucchi, D. Y. Oberli, & E. Kapon. *Quantum-dot exciton dynamics probed by photon-correlation spectroscopy*. Phys. Rev. B 73, 205321 (2006).
- [25] M. Grundmann & D. Bimberg. *Theory of random population for quantum dots*. Phys. Rev. B 55, 9740 (1997).
- [26] A. J. Bennett, M. A. Pooley, Y. Cao, N. Sköld, I. Farrer, D. A. Ritchie & A. J. Shields. *Voltage tunability of single-spin states in a quantum dot*. Nature Commun., 4, 1522 (2013)